Journal of
Materials Chemistry A

Using Phase Boundary Mapping to Resolve Discrepancies in the Mg_2Si-Mg_2Sn Miscibility Gap

Journal:	*Journal of Materials Chemistry A*
Manuscript ID	TA-ART-01-2021-000115.R1
Article Type:	Paper
Date Submitted by the Author:	15-Feb-2021
Complete List of Authors:	Orenstein, Rachel; Northwestern University Department of Materials Science and Engineering, ; Colorado School of Mines, Male, James; Northwestern University, Materials Science and Engineering Anand, Shashwat; Northwestern University, Materials Science and Engineering Toriyama, Michael; Northwestern University, Materials Science & Engineering Snyder, G.; Northwestern University, Materials Science

ARTICLE

Using Phase Boundary Mapping to Resolve Discrepancies in the Mg_2Si-Mg_2Sn Miscibility Gap

Received 00th January 20xx,
Accepted 00th January 20xx

DOI: 10.1039/x0xx00000x

Rachel Orenstein,[a] James P. Male,[a] Michael Toriyama,[a] Shashwat Anand,[a] and G. Jeffrey Snyder *[a]

Mg_2Si-Mg_2Sn compositions within the Mg-Si-Sn materials system have potential as inexpensive, efficient thermoelectrics. These compositions lie specifically along the pseudobinary line with compositions of $Mg_2Si_{1-x}Sn_x$. The alloying and possible nanostructuring within the miscibility gap could further increase the thermoelectric figure of merit (zT) for these materials. However, the solubility limits of the miscibility gap differ greatly in the literature. Such a discrepancy could be a result of differing Mg-compositions due to excess magnesium added during sample annealing. To define these limits better and explain the change in proposed solubility limits based on magnesium content, the three-phase regions on either side of the pseudobinary phase region are phase boundary mapped and defect energy calculations are performed. This study presents a new understanding of the Mg-Si-Sn ternary phase diagram around the pseudobinary phase region. The solubility limits on either side of the pseudobinary should be essentially identical between the Mg-rich and Mg-poor three-phase regions unless the system temperature is brought above about 565 °C, at which eutectic liquid $Mg_{0.9}Sn_{0.1}$ forms. This creates a second Mg-rich three-phase region which intersects the pseudobinary with a lower Sn solubility. Thus, samples prepared along the pseudobinary line are not well-defined thermodynamically when excess magnesium is added. Excess Mg can push the system into a new three phase region with $Mg_2Si_{1-x}Sn_x$ composition different from that of the true miscibility gap. This understanding presents new guidelines for evaluating the miscibility gap and assists strategies for microstructure engineering and thermoelectric material processing.

.

Introduction

Thermoelectric (TE) materials create electric voltage from a temperature difference (and vice versa). Thus, devices based on TE materials can be used for generating power and cooling.[1,2] Good TE materials have a high thermoelectric figure of merit, zT, which is directly dependent on the Seebeck coefficient and electrical conductivity and inversely dependent on the thermal conductivity from phonons and electrons. The interconnectedness of these properties makes increasing the figure of merit for many materials exceedingly difficult.[1,3] Solid solution alloying and nanostructuring are successful strategies for lowering the phonon thermal conductivity[4,5] as long as they do not similarly reduce the electrical conductivity.[6] Band engineering to achieve band convergence is another strategy to improve the Seebeck coefficient and electronic transport.[7] Such methods are frequently employed to improve thermoelectric materials like the Mg-Si-Sn ternary system, which is competitive with *n*-type PbTe-based thermoelectric materials, but without expensive, toxic elements.[8–11] The best compositions for thermoelectrics in this system lie along the pseudobinary phase line of Mg_2Si-Mg_2Sn (*i.e.* $Mg_2Si_{1-x}Sn_x$). High solubility of Sn and Si allow for thermal conductivity reduction by alloy scattering, and composition-dependent band engineering.[7,10,12] Further, a miscibility gap emerges in the pseudobinary below 800 °C, opening opportunities for further improvement by careful cultivation of nano-sized phases within the matrix phase.[8,11]

Alloying and controlling nanostructure formation requires an accurate description of the miscibility gap between Mg_2Si and Mg_2Sn. However, the current picture of the pseudobinary phase diagram reveals drastic disagreements in the boundaries of the miscibility gap (Figure 1).[13] These discrepancies hint at a significant experimental factor causing widely varied results between researchers. Repeatable, precise synthesis of the highest zT Mg-Si-Sn materials is impractical unless the phase diagram is understood, and its issues are resolved.

---

[a] Materials Science and Engineering, Northwestern University, Evanston, IL, USA

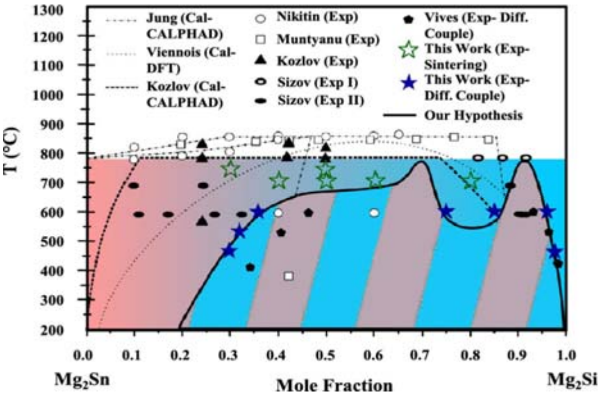

Figure 1: *Pseudobinary phase diagram summarizing previous work published on the boundaries of the miscibility gap of the Mg_2Si-Mg_2Sn system, from ref.* [13]

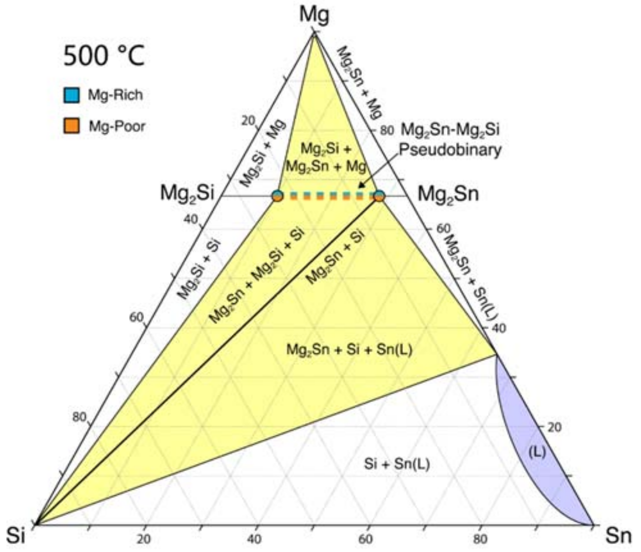

Figure 2*: Ternary phase diagram sketch (based on ref 14) showing the location of the ideal miscibility gap for the Mg_2Si-Mg_2Sn pseudobinary phase line assuming that Mg-rich and Mg-poor regions have equivalent solubility and all relevant phases are considered.*

In an attempt to achieve thermodynamic equilibrium and homogeneity for phase diagram analysis, previous researchers analyzing Mg_2Si-Mg_2Sn have annealed samples for several days in quartz glass ampules.[13] Magnesium reacts strongly with quartz, so magnesium loss occurs during anneals. Most researchers counteract this loss by adding excess elemental magnesium to the composition of the sample and/or to the sample environment during annealing.[13–15] Because of the variations in these practices, samples could end up with different degrees of magnesium-excess.

Further, a eutectic liquid with composition of approximately $Mg_{0.9}Sn_{0.1}$ forms near 565 °C.[16] Experiments involving elemental magnesium additions must carefully consider how the emergence of this eutectic Mg-rich liquid alters the shape of the phase boundaries near the pseudobinary compositions, especially given that many experiments bring the system temperature above 565 °C. Indeed, some authors have reported differences in phase formation after high temperature anneals depending on the use of excess magnesium.[15] This implies that the "known" ternary phase diagram (Figure 2) is not complete. Therefore, close attention should be paid to the effect of excess magnesium on the miscibility gap, which requires a better understanding of the phases and solubility limits on either side of the pseudobinary.

Phase boundary mapping is an experimental method for finding and defining the boundaries of one or more phase regions in a phase diagram using thermodynamic principles.[17] Under constant temperature and pressure, the Gibbs phase rule states that the degrees of freedom in a phase diagram region is equal to the number of components in the phase diagram minus the number of phases in the region. Thus, a three-phase region in a ternary phase diagram has zero degrees of freedom. This means that the three equilibrium phases with a fixed composition will appear as secondary phases in a sample made within the target three-phase region.[17] Preparing samples within the three-phase regions on either side of the Mg_2Si-Mg_2Sn pseudobinary line (yellow in Figure 2), can give the equilibrium-dependent compositional limits of the miscibility gap and define which compositions are candidates for achieving better *zT* through nanostructuring.[18]

In this work we investigated the limits of the miscibility gap for $Mg_2Si_{1-x}Sn_x$ by phase boundary mapping in the three-phase regions bordering the Mg_2Si-Mg_2Sn pseudobinary line. As a result, we found a previously undervalued three-phase region which terminates at the pseudobinary line when the eutectic liquid $Mg_{0.9}Sn_{0.1}$ is present. The presence of this phase region provides a possible explanation for the disagreement in miscibility gap solubility limits found in previous studies.

Results and Discussion

Thermodynamic Expectations for Phase Equilibrium

In the following section, we use simple thermodynamic arguments to suggest that the limits of the miscibility gap should be unaltered by changing phase equilibrium in this system. This general approach can be a useful tool for estimating the effects of phase boundary mapping on defect formation in other compounds where the dominant defect type is known or can be inferred with some confidence.

Alloying between Mg_2Sn and Mg_2Si is governed by exchanging Sn and Si atoms on the anion site ($Mg_2Si_{1-x}Sn_x$). Thus, composition changes along the corresponding pseudobinary line arise from the formation of uncharged tin-on-silicon (Sn_{Si}) or silicon-on-tin (Si_{Sn}) antisite defects, and any composition changes due to other defects, such as interstitials, are negligible.[19] The limits of Sn and Si solubility, or the boundaries of the miscibility gap, can then be understood by considering the formation energy of these antisite defects. If, for example, the Sn_{Si} defect formation energy is lower in one phase equilibrium than another, the lower energy region will have a larger concentration of Sn_{Si} defects and correspondingly higher Sn solubility.

Following the logic above, an initial estimate of the phase boundaries in the Mg-Si-Sn ternary phase diagram is made using simple thermodynamic arguments. For low temperatures, the relevant phase equilibria for Mg-rich conditions is (Mg+Mg_2Sn+Mg_2Si), or Region ‘1’ in Figure 3. On the Mg-poor (Si-rich) side this is (Si+Mg_2Si+Mg_2Sn) or Region ‘2’ in Figure 3. Regions ‘1a’ and ‘1b’, which are separated by a eutectic liquid phase that emerges at higher temperatures, are considered later in the text.

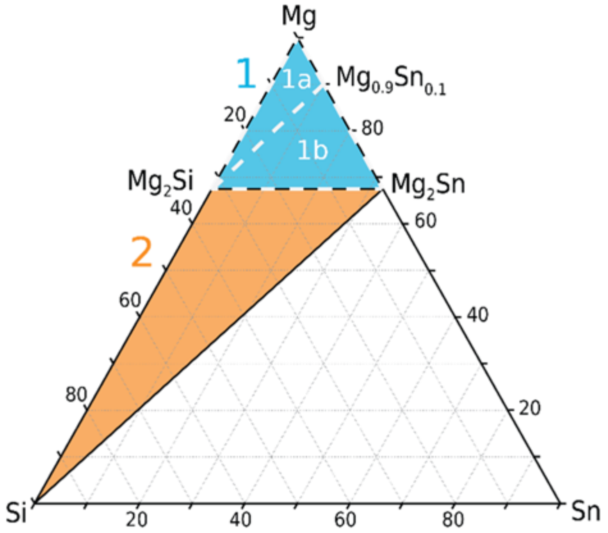

Figure 3: *Sketch showing phase regions in the Mg-Si-Sn system. Region 1 is the Mg-rich region around the* Mg_2Sn*-*Mg_2Si *pseudobinary (Mg+*Mg_2Sn*+*Mg_2Si*); Region 2 is the Mg-poor region (Si+*Mg_2Sn*+*Mg_2Si*); Region 1 is split into 1a (Mg+*Mg_2Si*+*$Mg_{0.9}Sn_{0.1}$*) and 1b (*$Mg_{0.9}Sn_{0.1}$*+*Mg_2Si*+*Mg_2Sn*) near 565 °C when eutectic liquid* $Mg_{0.9}Sn_{0.1}$ *forms.*

When adding Sn to Mg_2Si, the dominant defect for both Regions 1 and 2 is Sn_{Si}.[19] The formation enthalpy of a defect can be represented by the following equation[20]:

$$\Delta H_{Defect} = E_{Defects} - E_{Pristine} + \Delta H(D) \qquad (1)$$

Where $E_{Defects}$ is the energy of the defective structure, $E_{Pristine}$ is the energy of the perfect structure, and $\Delta H(D)$ is the molar enthalpy of the elements added or removed in the formation of the defect, in this case Si and Sn. The molar enthalpy can be represented as the difference between the chemical potentials, μ_i, of each element, *i*, written as $\mu_i^0 + \Delta\mu_i$.

$$\Delta H_{Sn_{Si}} = E_{Defects} - E_{Pristine} - (\mu_{Sn} - \mu_{Si})$$

$$\Delta H_{Sn_{Si}} = E_{Defects} - E_{Pristine} - \left(\mu_{Sn}^0 - \mu_{Si}^0\right) - (\Delta\mu_{Sn} - \Delta\mu_{Si})$$

The first three terms of the equation above are all constant (say *C*) for the defect, giving:

$$\Delta H_{Sn_{Si}} = C - (\Delta\mu_{Sn} - \Delta\mu_{Si}) \qquad (2)$$

Whereby we can directly compare defect formation energy, and thus Sn solubility, in Regions 1 and 2 by simply knowing the dominant defect type and estimating $\Delta\mu_{Sn}$ and $\Delta\mu_{Si}$.

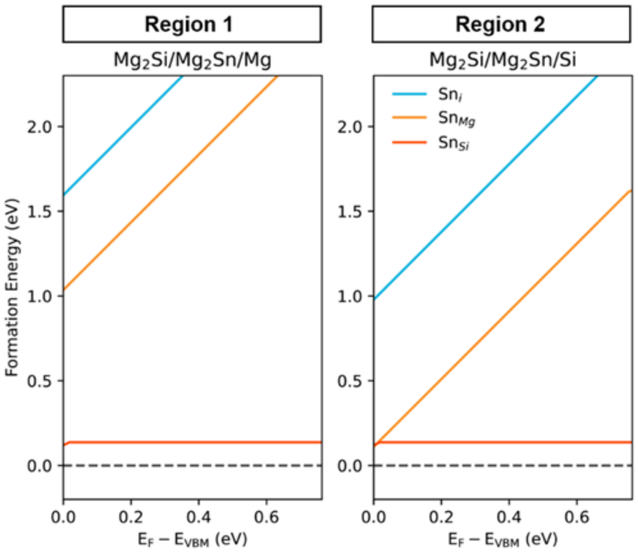

Figure 4: *Defect formation energies from Sn additions to* Mg_2Si *calculated for Regions 1 and 2 as a function of Fermi level (*E_F*) relative to the valence band maximum (*E_{VBM}*). Lower formation energy corresponds to higher defect concentrations; therefore,* Sn_{Si} *dominates in each phase and is the same in both Region 1 and Region 2.*

Using Equation 2, it is found below that the formation enthalpy for the Sn_{Si} defect must be similar between Regions 1 and 2, and therefore the solubility limits of the three-phase regions on either side of the pseudobinary line should not be very different. This assumes that slight changes in chemical potentials for elemental magnesium and silicon, such as from off-stoichiometry, are negligible and that the formation energies at 0 K are representative of the real system.[20]

Mg-rich region (1):

$$3\Delta H_{Mg_2Si} = 2\Delta\mu_{Mg} + \Delta\mu_{Si}$$

$$3\Delta H_{Mg_2Sn} = 2\Delta\mu_{Mg} + \Delta\mu_{Sn}$$

$$\Rightarrow (\Delta\mu_{Sn} - \Delta\mu_{Si}) = 3\Delta H_{Mg_2Sn} - 3\Delta H_{Mg_2Si}$$

Mg-poor region (2):

$$3\Delta H_{Mg_2Si} = 2\Delta\mu_{Mg} + \Delta\mu_{Si}$$

$$3\Delta H_{Mg_2Sn} = 2\Delta\mu_{Mg} + \Delta\mu_{Sn}$$

$$\Delta H_{Si} = \Delta\mu_{Si} = 0$$

$$\Rightarrow (\Delta\mu_{Sn} - \Delta\mu_{Si}) = \Delta\mu_{Sn} = 3\Delta H_{Mg_2Sn} - 3\Delta H_{Mg_2Si}$$

Thus, the chemical potential difference is the same for both regions resulting in identical defect energies $\Delta H_{Sn_{Si}}$ in Equation 2. This means that the equilibrium *x* in $Mg_2Si_{1-x}Sn_x$ for both Mg-rich and Mg-poor phase equilibria are the same. This will also be true for the Sn-rich side of the pseudobinary, $Mg_2Sn_{1-x}Si_x$.

The above analysis does not require detailed calculations or experiments, except that the dominant defect must be resolved. The defects associated with adding Sn to Mg_2Si are calculated from DFT shown in Figure 4 using a hybrid exchange-correlation functional, and their formation energies are plotted versus Fermi level (E_F). Sn_{Si} is the lowest energy defect at all calculated E_F's within the 0.76 eV bandgap. The defect is uncharged across most of the band gap but goes through a charge transition near the valence band maximum (VBM). Undoped Mg_2Si materials tend to be *n*-type (E_F far from the VBM), so the charge transition can be ignored for this analysis.[21] The Sn_{Si} formation energy is equivalent in Mg-rich (Region 1) and Mg-poor (Region 2) conditions, signifying identical solubilities in complete agreement with our prior conclusions from thermodynamics and algebra.

A eutectic liquid phase which we shall call "$Mg_{0.9}Sn_{0.1}$" forms near 565 °C. This splits Region 1 into Region 1a ($Mg+Mg_{0.9}Sn_{0.1}+Mg_2Si$) and Region 1b ($Mg_{0.9}Sn_{0.1}+Mg_2Si+Mg_2Sn$), as shown in Figure 3. While there are various experimental compositions[22,23] of this eutectic phase, the analyses that follow are independent of the exact composition. Though the eutectic $Mg_{0.9}Sn_{0.1}$ liquid is not stable at 0 K, we can administer the same treatment as above to determine whether the change in atomic chemical potentials from the introduction of a new Mg-rich phase influences $\Delta H_{Sn_{Si}}$ in Mg_2Si. In Region 1b:

$$3\Delta H_{Mg_2Si} = 2\Delta\mu_{Mg} + \Delta\mu_{Si}$$

$$3\Delta H_{Mg_2Sn} = 2\Delta\mu_{Mg} + \Delta\mu_{Sn}$$

$$10\Delta H_{Mg_{0.9}Sn_{0.1}} = 9\Delta\mu_{Mg} + \Delta\mu_{Sn}$$

$$\Rightarrow (\Delta\mu_{Sn} - \Delta\mu_{Si}) = 3\Delta H_{Mg_2Sn} - 3\Delta H_{Mg_2Si}$$

And a similar estimate can be made for Region 1a. Because elemental magnesium is one of the equilibrium phases, the change in chemical potential for magnesium, and therefore the formation energy, equals zero.

$$\Delta H_{Mg} = \Delta\mu_{Mg}$$

$$3\Delta H_{Mg_2Si} = 2\Delta\mu_{Mg} + \Delta\mu_{Si}$$

$$10\Delta H_{Mg_{0.9}Sn_{0.1}} = 9\Delta\mu_{Mg} + \Delta\mu_{Sn}$$

$$\Rightarrow (\Delta\mu_{Sn} - \Delta\mu_{Si}) = 10\Delta H_{Mg_{0.9}Sn_{0.1}} - 3\Delta H_{Mg_2Si}$$

This results in the following equation for the Sn_{Si} defect formation enthalpy for Region 1a:

$$\Delta H^{1a}_{Sn_{Si}} = C - \left(10\Delta H_{Mg_{0.9}Sn_{0.1}} - 3\Delta H_{Mg_2Si}\right)$$

This expression can be compared to the expression for the defect formation energy of Region 1b, giving the following relationship.

$$\Delta H^{1a}_{Sn_{Si}} - \Delta H^{1b}_{Sn_{Si}} = 3\Delta H_{Mg_2Sn} - 10\Delta H_{Mg_{0.9}Sn_{0.1}} \qquad (3)$$

For the solubility of Sn_{Si} in Region 1a to be lower than that of Region 1b, $(\Delta H^{1a}_{Sn_{Si}} - \Delta H^{1b}_{Sn_{Si}})$ must be greater than zero, giving the inequality in equation 4.

$$\Rightarrow \frac{10}{3} < \frac{\Delta H_{Mg_2Sn}}{\Delta H_{Mg_{0.9}Sn_{0.1}}} \qquad (4)$$

By definition, for $Mg_{0.9}Sn_{0.1}$ to "break" the convex hull between Mg and Mg_2Sn (become low enough in energy that it becomes stable), Equation 4 must be true. Assuming the relative difference in formation energy between Mg_2Sn and $Mg_{0.9}Sn_{0.1}$ stays similar at higher temperatures, and the inequality remains true, the solubility of Region 1a is expected to be lower than Region 1b above 565 °C, as in Figure 9.

The basic algebra carried out in this section estimates that the shape of the miscibility gap should be independent of magnesium concentration when two of the three phases in equilibrium are Mg_2Si and Mg_2Sn. Above 565 °C, Sn solubility in Mg_2Si can be relatively lower in the three-phase region in equilibrium with the $Mg_{0.9}Sn_{0.1}$ eutectic liquid and elemental magnesium. Computationally determined energies of formation for Sn_{Si} are consistent with this result.

Experimental Results of Phase Boundary Mapping

Experimental phase boundary mapping was carried out by synthesizing samples with nominal compositions in Regions 1 and 2 (Figure 3), annealing at high temperature, then examining the composition of the secondary phases in the samples. We ensured the correct three phase equilibrium by first performing X-ray diffraction (XRD) on each sample, then using energy dispersive spectroscopy (EDS) to determine the specific compositions of each secondary phase.

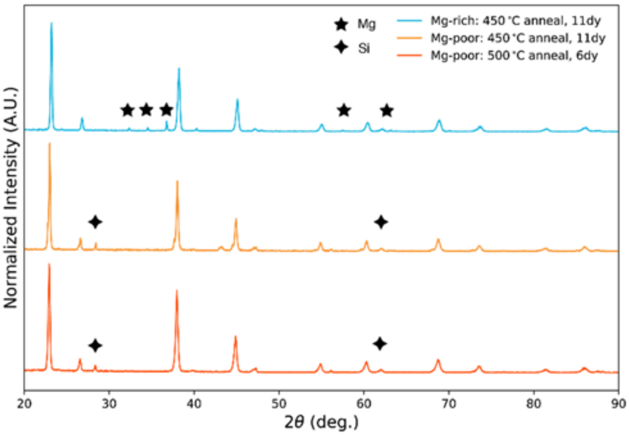

***Figure 5**: Pellet X-ray diffraction (XRD) peaks for Mg-rich and Mg-poor samples after annealing at 450 °C or 500 °C (Copper Kα source). The main pattern is Mg_2Si and Mg_2Sn while impurities of magnesium (stars) and silicon (diamonds) are marked.*

The X-ray diffraction pattern for each region matches the main peaks of Mg_2Si and Mg_2Sn diffraction patterns (Figure 5). This, along with the presence of elemental impurity peaks (magnesium peaks for Mg-rich and silicon peaks for Mg-poor) in the diffraction patterns, indicates that the compositions are within the target ranges and that the expected secondary phases are present.

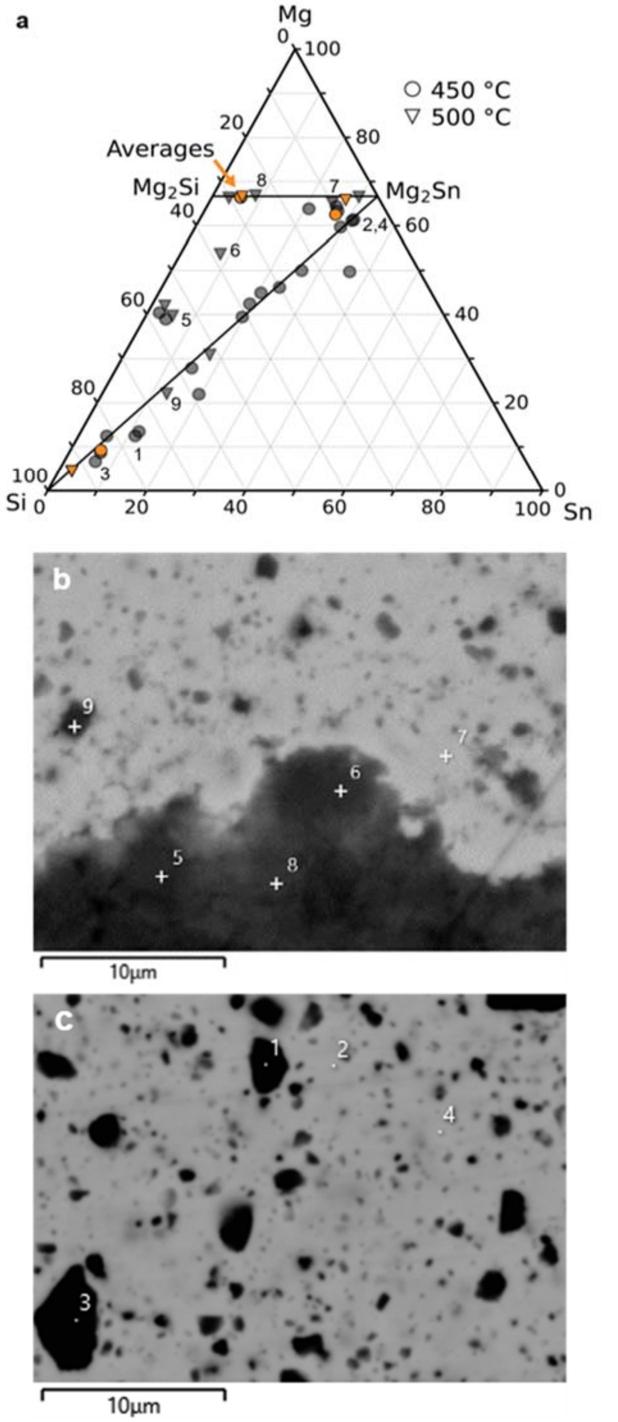

Figure 6: ***a.*** *Ternary plot of measured phase compositions for Mg-poor sample after annealing at 500 °C for 6 days (orange indicates average of surrounding points).* ***b-c.*** *Example electron images showing microstructure for samples annealed at* ***b.*** *450 °C and* ***c.*** *500 °C. Annotations indicate the locations of the compositions taken in* ***a.***

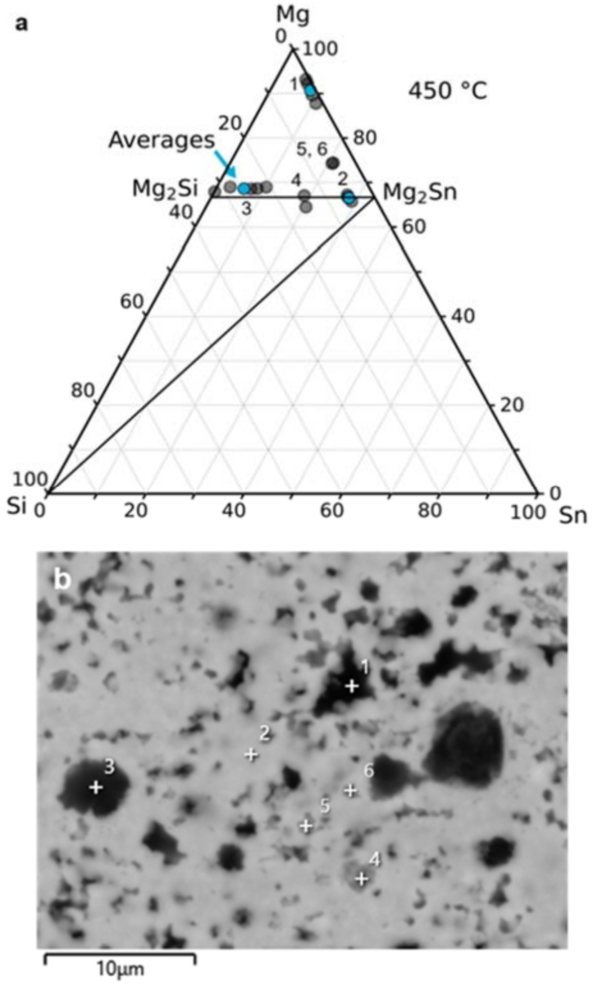

Figure 7*:* ***a.*** *Ternary plot of measured phase compositions for Mg-rich sample after annealing at 450 °C for 11 days (blue indicates average of surrounding points).* ***b.*** *Example electron images showing microstructure with annotations indicating the locations of the compositions taken in* ***a****.*

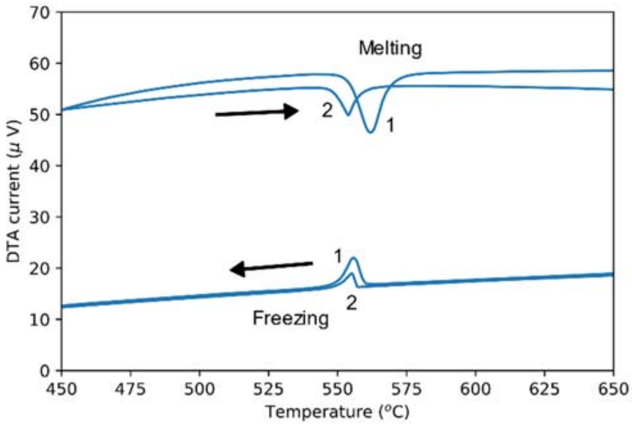

Figure 8*: Differential thermal analysis (DTA) cycle data, DTA current (µV) vs. Temperature (°C) for two cycles (peaks labeled "1" and "2") from 30 °C – 800 °C, showing the melting and refreezing of eutectic* $Mg_{0.9}Sn_{0.1}$ *liquid near 560 °C.*

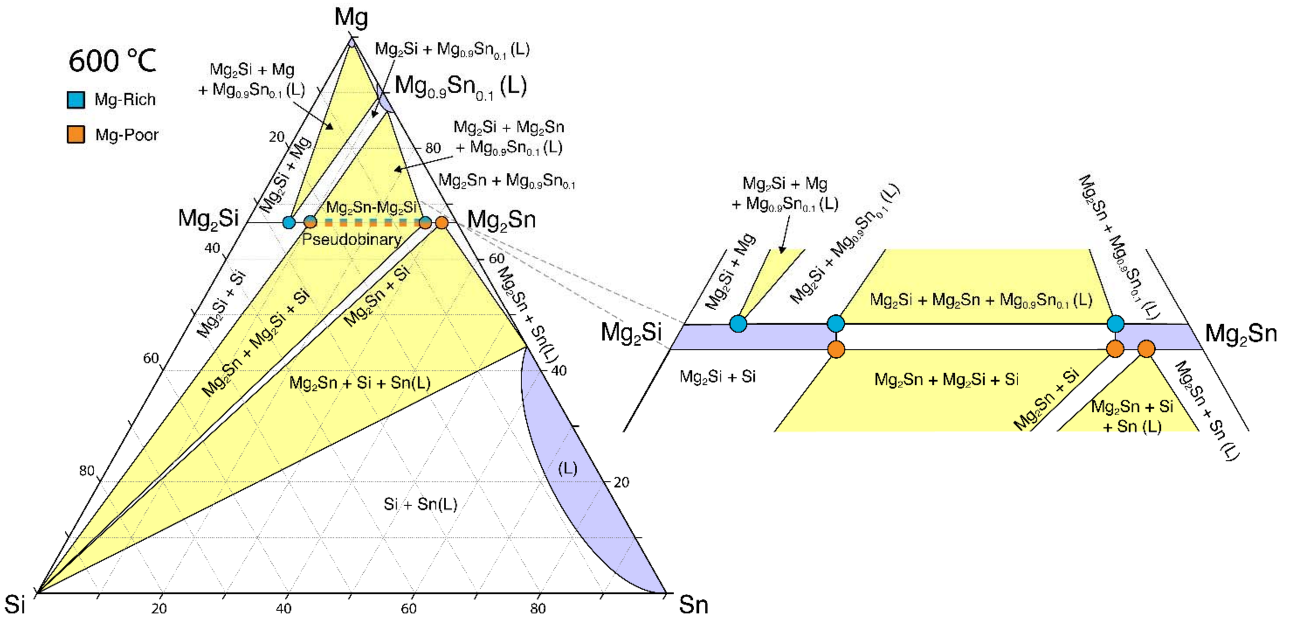

Figure 9*: Sketch of proposed 600 °C ternary phase diagram surrounding the Mg_2Si-Mg_2Sn pseudobinary phase line which shows the similar maximum x in $Mg_2Si_{1-x}Sn_x$ & $Mg_2Si_xSn_{1-x}$ for both Mg-rich samples (blue dots) and Sn-rich compositions (orange dots) that are in equilibrium with Mg_2Si and Mg_2Sn. At this temperature, equilibrium with elemental Mg will require entering a new 3-phase region defined by Mg + $Mg_{0.9}Si_{0.1}$ + Mg_2Si where the $Mg_2Si_{1-x}Sn_x$ composition (value of x) will be different than that found in the pseudobinary. Similarly, entering the Mg_2Sn+Si+Sn(L) region will result in a lower Si solubility than the three-phase region directly bordering the pseudobinary.*

The XRD patterns suggest that all samples are equilibrated, although intermediate compositions still show up in the EDS spectra (Figures 6 and 7). The continued presence of seemingly “non-equilibrium” compositions indicates that the diffusion in these samples is slower than expected. Fine nanostructures of secondary phases within other larger precipitates has been noted before, even after long anneals.^{13} In our study, these nanostructures within the precipitates did not grow enough to be resolved at the imaged magnification. At the magnification used, the EDS detector would register these mixtures of nanostructures as an intermediate composition between the constituents. Additionally, the accuracy of EDS is insufficient to show exact compositions. However, averaging multiple EDS measurements of the phases expected in both three-phase equilibrium regions paints a clear picture of the phase regions in question (Figures 6 and 7), and distinct phase boundaries emerge (Figure 9).

The appearance of the $Mg_{0.9}Sn_{0.1}$ composition measured at 450 °C rather than elemental Mg is a surprising result. This composition represents a mixture of Mg_2Sn and Mg after solidification and phase separation of a eutectic $Mg_{0.9}Sn_{0.1}$ liquid. This study was designed to keep all synthesis temperatures below the expected 565 °C eutectic melting point; however, EDS measurements indicate that a eutectic liquid was formed after pressing the powders into pellets. To check whether the eutectic melting temperature was lower than expected, differential thermal analysis (DTA) of a Mg-rich powder sample was performed. The DTA signal shows peaks corresponding to melting and freezing above 550 °C (Figure 7). This is counterintuitive to the appearance of the eutectic liquid in these samples, however even an error of 10% in the pressing temperature would reasonably allow for the appearance of the eutectic liquid phase in these samples.

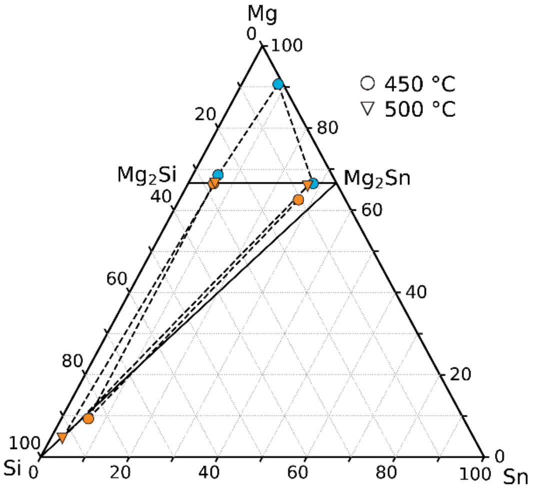

Figure 10*: Average of measured phase compositions from samples made within the Mg-rich and Mg-poor 3-phase regions bordering the pseudobinary between Mg_2Si and Mg_2Sn. Results are shown for samples annealed at 450 °C or 500 °C.*

Figure 10 shows the experimental phase regions determined from phase boundary mapping, representing the Mg-rich and Mg-poor regions. As predicted by the thermodynamic analysis discussed above, the solubility limits of each phase match very well along the Mg_2Si-Mg_2Sn pseudobinary. The presence of the $Mg_{0.9}Sn_{0.1}$ phase as one of the three coexisting phases in the Mg-rich region suggests that another three-phase region (Region 1a) likely exists in the Mg-rich space, which can also intersect with the pseudobinary (Figure 9) at a different tin solubility. This difference in tin solubility between the two Mg-rich phases (Figure 9) could explain the reported variations in the miscibility gap. If a sample with composition along the pseudobinary line becomes Mg-rich due to added excess magnesium during annealing such that the global system composition (sample plus excess magnesium) lies within Region 1a ($Mg+Mg_{0.9}Sn_{0.1}+Mg_2Si$), it would result in a lower value for the solubility limit on the Mg_2Si side of the pseudobinary, therefore changing the apparent boundaries of the miscibility gap. Any effects on thermoelectric properties resulting from the eutectic $Mg_{0.9}Sn_{0.1}$ phase are beyond the scope of this work but may be a useful topic in future studies. Further, the same occurrence may be present on the Mg_2Sn side of the pseudobinary, where a eutectic liquid also forms, and might explain why discrepancies occur on both sides of the pseudobinary. In this case, significant magnesium loss could shift the phase equilibrium to $Mg_2Sn+Si+Sn(L)$ rather than the expected $Si+Mg_2Si+Mg_2Sn$ equilibrium, leading to an underestimation of Si solubility (see right hand side of Figure 9). The exact value of the solubility limit of the Mg-rich ($Mg+Mg_{0.9}Sn_{0.1}+Mg_2Si$) phase at the pseudobinary line can be determined through further phase boundary mapping of this unexplored phase region.

Conclusions

The miscibility gap seen on the pseudobinary phase line between Mg_2Si and Mg_2Sn is highly contested in literature. In principle, because Sn on a Si site is the dominant defect in Mg_2Si and it is in equilibrium with Mg_2Sn, the solubility of Sn in Mg_2Si should be the same in both Mg-rich and Mg-poor equilibria. Thus, true equilibrium experiments should show little discrepancy.

However, experiments often include additions of excess elemental magnesium to prevent magnesium loss, which brings the system out of equilibrium. In these instances, a different composition of $Mg_2Si_{1-x}Sn_x$ forms above approximately 565 °C when elemental magnesium is in equilibrium with Mg_2Si (Figure 9) because of the appearance of the eutectic liquid $Mg_{0.9}Sn_{0.1}$, as evidenced by differential thermal analysis results (Figure 8).

The experimental phase regions determined in Figure 10 match two important results stemming from basic thermoelectric considerations: 1) the composition of the Mg-rich and Mg-poor Mg_2Sn and Mg_2Si phases match nearly exactly as predicted by thermodynamic arguments, and 2) the Mg-rich phase can be in equilibrium with the eutectic liquid $Mg_{0.9}Sn_{0.1}$ phase, which allows for a second Mg-rich three-phase region ($Mg+Mg_2Si+Mg_{0.9}Sn_{0.1}$) (Figure 3). This phase is neglected in several experimental studies of the ternary system but can affect the apparent shape of the miscibility gap when annealing samples on the pseudobinary near Mg_2Si with elemental magnesium.

This difference in tin content between the two Mg-rich phases could explain the reported variations in the miscibility gap. If a sample along the pseudobinary line becomes Mg-rich due to added excess magnesium during annealing such that it lies within the Mg-rich ($Mg+Mg_{0.9}Sn_{0.1}+Mg_2Si$) three-phase region (Figure 9), it would result in a lower value for the solubility limit on the Mg_2Si side of the pseudobinary, therefore changing the boundaries of the miscibility gap. The exact value of the solubility limit of the Mg-rich ($Mg + Mg_{0.9}Sn_{0.1}+Mg_2Si$) phase at the pseudobinary line can be determined through further phase boundary mapping of this unexplored phase region. Additionally, the presence of a liquid is known for Mg-poor compositions on the Mg_2Sn side of the pseudobinary line. Applying the same approach to the other side of the pseudobinary will likely reveal that similar discrepancies can arise due to magnesium loss, explaining discrepancies on both sides of the current Mg_2Si-Mg_2Sn pseudobinary picture.

Understanding the limits of the miscibility gap is important for future development of $Mg_2Si_xSn_{1-x}$ thermoelectric materials. By exploring the phase regions surrounding the pseudobinary Mg_2Si-Mg_2Sn system from an isothermal ternary plot perspective, we demonstrate the importance of phase boundary mapping and phase equilibrium in phase diagram experiments and synthesis.

Methods

Experimental Methods

To properly examine the difference in solubility limit on either side of the Mg_2Si-Mg_2Sn pseudobinary phase line, compositions were synthesized within the three phase regions on either side of the pseudobinary line. The chosen compositions of $Mg_{60}Si_{18}Sn_{22}$ (Mg-poor region) and $Mg_{74}Si_6Sn_{20}$ (Mg-rich region) fall inside these regions in Figure 2 at 500 °C. X-ray diffraction and microscopy show evidence that the compositions of the samples are within the desired three-phase regions after equilibrating.

Each sample was synthesized by ball milling and hot pressing. Pure magnesium (Alfa Aesar 99.99%, flakes), tin (Alfa Aesar 99.99%, shot), and silicon (Sigma-Aldrich 99.95%, chunks) were first measured out into stainless steel ball mill jars in an argon-filled glovebox. The jars were then placed into a Spex 8000D high energy ball mill for a total of 210 minutes in increments of 90 min. – 90 min. – 30 min. During ball milling, which works by mechanically alloying the elements[24], some material collects in chunks on all surfaces of the jar which can prevent full reactions and homogeneity. This material was chipped off the jar's surfaces and remixed between ball milling intervals to assist reactions. The fine powder was then measured out into graphite molds (12.7 mm) and pressed in an induction heated rapid hot press under vacuum. During pressing, the sample was heated to 500 °C and held under 60 MPa for 60 minutes under Argon flow.

X-ray diffraction analysis was performed on pressed pellets in reflection mode using Cu-α radiation with a 2θ range between 10° and 90°. Selected samples were also annealed in a furnace to ensure equilibrium. All samples were coated in Boron Nitride spray and then sealed in three-times carbon-coated quartz tubes under vacuum along with 0.5 grams of powder of the nominal starting composition to reduce composition changes from diffusion of magnesium into the quartz ampule. One set of samples (Mg-rich and Mg-poor) was annealed at 450 °C for 11 days and a second set at 500 °C for 6 days. Samples were imaged & EDS spectra were taken both before and after annealing using a Hitachi S-3400N-II Scanning Electron Microscope (SEM) and an Oxford INCA SiLi EDS system. The SEM used an accelerating voltage of 20kV, and probe currents of 50 on a scale of 0 to 100 (secondary electron detection) and 70 or 80 (backscatter electron detection). Differential Thermal Analysis (DTA) was performed using the Netzsch Jupiter Simultaneous Thermal Analysis system on a sample of the powder for the Mg-rich region to identify the eutectic liquid phase formation. The powder sample was sealed under vacuum in a carbon-coated quartz capillary tube. Two heating and cooling cycles were performed over a temperature range of 30–800 °C.

Computational Methods

First-principles Density Functional Theory-based defect calculations were performed using the Vienna ab-initio simulation package (VASP)[25–27] with the projector-augmented wave method[28,29]. The plane-wave energy cutoff was set to 500 eV for all calculations. A 96-atom supercell of Mg2Si was used for all defect calculations, where the formation energy ΔH_{D^q} for a defect D^q with charge state q was calculated using the formula

$$\Delta H_{D^q} = E_{D^q} - E_{Host} - \sum n_i \mu_i + qE_F + E_{Corr}$$

where E_{D^q} and E_{Host} are the total energies of the supercell with and without the defect respectively, $\sum n_i \mu_i$ accounts for the atomic chemical potentials, E_F is the Fermi level, and E_{Corr} is the energy correction determined using the method of Freysoldt[30]. We use the hybrid functional due to Heyd, Scuseria, and Ernzerhof[31–33], where we set the fraction of exact Hartree-Fock exchange to 0.37. This yields a band gap and lattice constant of 0.76 eV and 6.32 Å respectively, in close agreement with the experimental values of 0.78 eV and 6.35 Å.[34]

Author Contributions

RO carried out the experiments and drafted the manuscript with input from JM. JM and GJS also contributed to the preparation of the manuscript, and JM contributed to the figure presentation. JM and SA developed the thermodynamic arguments, and MT carried out computations and provided the related figure. GJS supervised the project. All authors helped shape the research and analysis.

Conflicts of interest

There are no conflicts of interest to declare.

Acknowledgements

We acknowledge NSF DMREF award #1729487 and the support of award 70NANB19H005 from U.S. Department of Commerce, National Institute of Standards and Technology as part of the Center for Hierarchical Materials Design (CHiMaD). We thank Johannes de Boor and Mohammad Yasseri for helpful discussions. This work made use of the IMSERC X-RAY facility at Northwestern University, which has received support from the Soft and Hybrid Nanotechnology Experimental (SHyNE) Resource (NSF ECCS-2025633), and Northwestern University. Additionally, this work made use of the EPIC facility of Northwestern University's NUANCE Center, supported by the SHyNE Resource (NSF ECCS-2025633), the IIN, and Northwestern's MRSEC program (NSF DMR-1720139). MT acknowledges support from the United States Department of Energy through the Computational Science Graduate Fellowship (DOE CSGF) under Grant Number DE-SC0020347. This research was supported in part through the computational resources and staff contributions provided for the Quest high performance computing facility at Northwestern University which is jointly supported by the Office of the Provost, the Office for Research, and Northwestern University Information Technology.

Notes and references

1 G. J. Snyder and E. S. Toberer, *Nat. Mater.*, 2008, **7**, 105–114.
2 F. J. DiSalvo, *Science*, 1999, **285**, 703–706.
3 L.-D. Zhao, V. P. Dravid and M. G. Kanatzidis, *Energy Env. Sci*, 2014, **7**, 251–268.
4 M. G. Kanatzidis, *Chem. Mater.*, 2010, **22**, 648–659.
5 R. Gurunathan, R. Hanus and G. J. Snyder, *Mater. Horiz.*, 2020, **7**, 1452–1456.
6 H. Wang, A. D. LaLonde, Y. Pei and G. J. Snyder, *Adv. Funct. Mater.*, 2013, **23**, 1586–1596.
7 W. Liu, X. Tan, K. Yin, H. Liu, X. Tang, J. Shi, Q. Zhang and C. Uher, *Phys. Rev. Lett.*, 2012, **108**, 166601.
8 N. Farahi, S. Prabhudev, G. A. Botton, J. R. Salvador and H. Kleinke, *ACS Appl. Mater. Interfaces*, 2016, **8**, 34431–34437.
9 W. Li, L. Lindsay, D. A. Broido, D. A. Stewart and N. Mingo, *Phys. Rev. B*, 2012, **86**, 174307.
10 V. K. Zaitsev, M. I. Fedorov, E. A. Gurieva, I. S. Eremin, P. P. Konstantinov, A. Yu. Samunin and M. V. Vedernikov, *Phys. Rev. B*, 2006, **74**, 045207.
11 J. de Boor, T. Dasgupta, H. Kolb, C. Compere, K. Kelm and E. Mueller, *Acta Mater.*, 2014, **77**, 68–75.
12 T. Dasgupta, C. Stiewe, J. de Boor and E. Müller, *Phys. Status Solidi A*, 2014, **211**, 1250–1254.
13 M. Yasseri, A. Sankhla, H. Kamila, R. Orenstein, D. Y. N. Truong, N. Farahi, J. de Boor and E. Mueller, *Acta Mater.*, 2020, **185**, 80–88.
14 D. Kato, K. Iwasaki, M. Yoshino, T. Yamada and T. Nagasaki, *J. Solid State Chem.*, 2018, **258**, 93–98.
15 G. K. Goyal and T. Dasgupta, *J. Electron. Mater.*, 2018, **47**, 2066–2072.
16 Y.-B. Kang and A. D. Pelton, *Calphad*, 2010, **34**, 180–188.
17 S. Ohno, K. Imasato, S. Anand, H. Tamaki, S. D. Kang, P. Gorai, H. K. Sato, E. S. Toberer, T. Kanno and G. J. Snyder, *Joule*, 2018, **2**, 141–154.
18 N. A. Heinz, T. Ikeda, Y. Pei and G. J. Snyder, *Adv. Funct. Mater.*, 2014, **24**, 2135–2153.
19 X. Han and G. Shao, *J. Appl. Phys.*, 2012, **112**, 013715.
20 S. Anand, J. P. Male, C. Wolverton and J. Snyder, *Unpubl. Work*.
21 M. Akasaka, T. Iida, A. Matsumoto, K. Yamanaka, Y. Takanashi, T. Imai and N. Hamada, *J. Appl. Phys.*, 2008, **104**, 013703.

22 A. A. Nayeb-Hashemi and J. B. Clark, *Bull. Alloy Phase Diagr.*, 1984, **5**, 466–476.

23 L. Povlova and K. Poyarkov, *Russ J Phys Chem*, 1982, **56**, 183–185.

24 A. Sankhla, A. Patil, H. Kamila, M. Yasseri, N. Farahi, E. Mueller and J. de Boor, *ACS Appl. Energy Mater.*, 2018, **1**, 531–542.

25 G. Kresse, *J. Non-Cryst. Solids*, 1995, **192–193**, 222–229.

26 G. Kresse and J. Furthmüller, *Comput. Mater. Sci.*, 1996, **6**, 15–50.

27 G. Kresse and J. Furthmüller, *Phys. Rev. B*, 1996, **54**, 11169–11186.

28 P. E. Blöchl, *Phys. Rev. B*, 1994, **50**, 17953–17979.

29 G. Kresse and D. Joubert, *Phys. Rev. B*, 1999, **59**, 1758–1775.

30 C. Freysoldt, J. Neugebauer and C. G. Van de Walle, *Phys. Rev. Lett.*, 2009, **102**, 016402.

31 J. Heyd, G. E. Scuseria and M. Ernzerhof, *J. Chem. Phys.*, 2003, **118**, 8207–8215.

32 J. Heyd and G. E. Scuseria, *J. Chem. Phys.*, 2004, **121**, 1187–1192.

33 A. V. Krukau, O. A. Vydrov, A. F. Izmaylov and G. E. Scuseria, *J. Chem. Phys.*, 2006, **125**, 224106.

34 R. G. Morris, R. D. Redin and G. C. Danielson, *Phys. Rev.*, 1958, **109**, 1909–1915.